

# PROCEEDINGS OF SPIE

[SPIDigitalLibrary.org/conference-proceedings-of-spie](https://spiedigitallibrary.org/conference-proceedings-of-spie)

## Video rate spectroscopy via Fourier-spectral-multiplexing

Chao Deng, Xuemei Hu, Jinli Suo, Yuanlong Zhang, Zhili Zhang, et al.

Chao Deng, Xuemei Hu, Jinli Suo, Yuanlong Zhang, Zhili Zhang, Qionghai Dai, "Video rate spectroscopy via Fourier-spectral-multiplexing," Proc. SPIE 10889, High-Speed Biomedical Imaging and Spectroscopy IV, 108891L (4 March 2019); doi: 10.1117/12.2506153

**SPIE.**

Event: SPIE BiOS, 2019, San Francisco, California, United States

# Video rate spectroscopy via Fourier-spectral-multiplexing

Chao Deng<sup>a,b</sup>, Xuemei Hu<sup>a</sup>, Jinli Suo<sup>a</sup>, Yuanlong Zhang<sup>a</sup>, Zhili Zhang<sup>b</sup>, and Qionghai Dai<sup>a</sup>

<sup>a</sup>Department of Automation, Tsinghua University, Beijing, 100084, China

<sup>b</sup>High-Tech Institute of Xi'an, Xi'an, 710025, China

## ABSTRACT

Spectroscopy is an important tool having already been applied in various research fields, but still limited in observation of dynamic scenes. In this paper, we propose a video rate spectroscopy via Fourier-spectral-multiplexing (FSM-VRS) which exploits both spectral and spatial sparsity. Under the computational imaging scheme, the hyperspectral datacube is first modulated by several broadband bases, and then mapped into different regions in the Fourier domain. The encoded image compressed both in spectral and spatial are finally collected by a monochrome detector. Correspondingly, the reconstruction is essentially a Fourier domain extraction and spectral dimensional back projection with low computational load. The encoding and decoding process of the FSM-VRS is simple thus can be implemented in a low cost manner. The temporary resolution of the FSM-VRS is only limited by the camera frame rate. We demonstrate the high performance of our method by quantitative evaluation on simulation data and build a prototype system experimentally for further validation.

**Keywords:** Hyperspectral imaging, Fourier spectral multiplexing, snapshot, monochrome detector

## 1. INTRODUCTION

Hyperspectral imaging aims to capture the details of the spectra of natural scene. It is playing great roles in both scientific research and engineering applications, such as military security,<sup>1,2</sup> environmental monitoring,<sup>3</sup> biological science,<sup>4,5</sup> medical diagnosis,<sup>6,7</sup> scientific observation,<sup>8,9</sup> and many other fields.<sup>10-12</sup>

The typical way to perform snapshot hyperspectral imaging is mapping different spectral bands (either single narrow band or multiplexed ones) to different positions and then collecting them by one or more detectors. So far, various methods have been proposed to implement such band mapping. The integral field spectroscopy (IFS),<sup>13,14</sup> multispectral beamsplitting (MSBS),<sup>15</sup> image replicating image spectrometer (IRIS)<sup>16,17</sup> and multispectral sagnac interferometer (MSI)<sup>18</sup> are the paradigms directly using stacked optical components to split spectral channels, which complicate the system and impose strict limitation on the light path building. Another drawback of the direct mapping method is limited spectral band number. For example, the spectral band number of MSBS is dependent on the beam splitter which is upper limited by 4, and the spectral resolution of IRIS is limited to 16 wavelength bands due to lack of large-format sufficient-birefringence Wollaston polarizers. In comparison, computed tomography imaging spectrometer (CTIS),<sup>19</sup> multi-aperture filtered camera (MAFC),<sup>20</sup> image mapping spectrometry (IMS)<sup>21</sup> and snapshot hyperspectral imaging Fourier transform (SHIFT)<sup>22</sup> are more compact but need customized components, which is usually expensive and of high fabrication difficulty. Introducing new reconstruction algorithms might inspire new imaging schemes and raise the final performance. The coded aperture snapshot spectral imager (CASSI)<sup>23</sup> is the first imager exploiting the compressive sensing theory to recover hyperspectrum. Getting rid of simple combination of optical elements, this method demands careful calibration and heavy computational load, which limits its broad applications in the scenarios where on-line reconstruction is needed. In sum, a snapshot spectral imager, with simple implementation, low computation load, and high reconstruction performance are worth studying. Making use of both the spatial<sup>24,25</sup> and spectral sparsity of the natural hyperspectral data, we propose a snapshot Fourier-Spectral-Multiplexing (FSM) method for hyperspectral imaging using a monochrome camera. Our snapshot hyperspectral imaging method can achieve high spatial-spectral resolution and high frame rate, with low cost setup and computational workload.

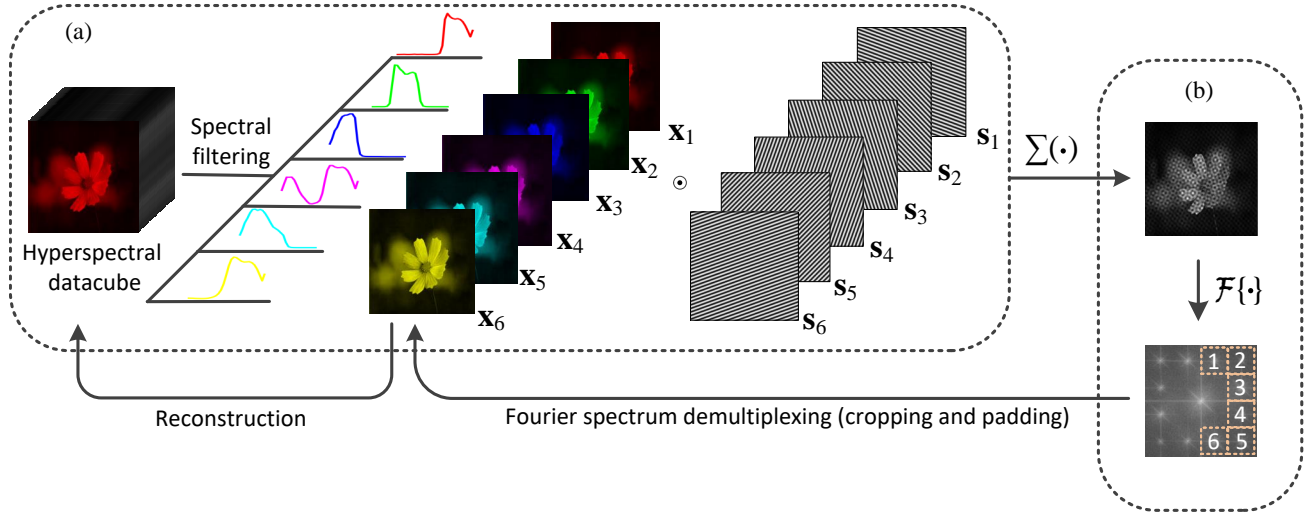


Figure 1. The scheme of the proposed hyperspectral imaging system. The hyperspectral data is spectrally filtered and projected into six images:  $\mathbf{x}_1, \mathbf{x}_2, \dots, \mathbf{x}_6$ , and then codified by six sinusoidal patterns  $\mathbf{s}_1, \mathbf{s}_2, \dots, \mathbf{s}_6$ , respectively. The six sinusoidal patterns shift the Fourier distribution of six projected images away from the origin into six different regions, and the gray scale camera captures the modulated images in an add-up way. The hyperspectral images are reconstructed through a two-stage method, including: Fourier spectrum demultiplexing and linear system reconstruction.

## 2. METHOD

The architecture for the snapshot hyperspectral imaging is shown in Fig. 1(a), including both encoding and decoding modules. During encoding, the 3D hyperspectral data cube is sequentially projected to a low dimensional space after going through a series of wide-band spectral filters, denoting as  $\mathbf{x}_1, \mathbf{x}_2, \dots, \mathbf{x}_J$ . Since the spectrum of natural scenes are of low intrinsic dimension, the hyperspectral datacube can be denoted as the linear summation of a few spectral basis. To ensure that the reconstruction problem is well posed, the number of color filters is equal to that of spectral basis. Statistics tells that six bases are sufficient for high fidelity hyperspectral data representation (see<sup>26</sup>), so here we set  $J$  as 6. Then the projections are modulated by different sinusoidal patterns  $\mathbf{s}_1, \mathbf{s}_2, \dots, \mathbf{s}_J$ , respectively. Mathematically, the sinusoidal modulation is represented as point-wise product “ $\odot$ ”, and would shift the Fourier spectrum of each projection into a specific region in the Fourier domain. The sinusoidal patterns are designed to ensure few overlap among the Fourier distributions of  $\{\mathbf{x}_i\}$ . Finally, the fast coded image is recorded by a gray scale camera in an add-up way as shown in the Fig. 1(a). Corresponding to the coding procedure, the decoding is straightforward. We first transform the captured image to the Fourier domain, and extracting the Fourier spectrum of each projection  $\mathbf{x}_i$  according to the shifting effect of the corresponding sinusoidal modulation  $\mathbf{s}_i$ . Then we transform the separated Fourier spectrum back to the spatial domain. Finally, we back project the reconstructions to the high dimensional data cube by solving a linear system. The Fourier spectrum demultiplexing includes two processes: Fourier spectrum cropping and zero padding to the original resolution.

Mathematically, though going through the  $i$ th spectral filter, the spectrum of the target scene is filtered with the corresponding spectral transmission, which can be represented as

$$\mathbf{x}_i = \int_{\lambda} \mathbf{I}_i(\lambda) \mathbf{r}(\lambda) d\lambda, \quad (1)$$

in which  $\mathbf{I}_i(\lambda)$  is the spectrum transmission of the  $i$ th spectral filter and  $\mathbf{r}(\lambda)$  denoting the spectrum reflectance/transmission. Here we omit 2D spatial coordinate for brevity. Statistically, the spectra of the natural

Send correspondence to Jinli Suo: jlsuo@tsinghua.edu.cn

materials can be represented as a linear summation of a few (e.g.,  $J=6$ ) characteristic spectral basis,<sup>27</sup> i.e.

$$\mathbf{r}(\lambda) = \sum_{j=1}^J \alpha_j \mathbf{b}_j(\lambda), \quad (2)$$

where  $\mathbf{b}_j$  is the  $j$ th spectral basis, and  $\alpha_j$  is the corresponding coefficients. Substituting Eq. (2) into Eq. (1),<sup>28,29</sup> we could get

$$\mathbf{x}_i = \sum_{j=1}^J \alpha_j \int_{\lambda} \mathbf{I}_i(\lambda) \mathbf{b}_j(\lambda) d\lambda. \quad (3)$$

In Eq. (3),  $\mathbf{I}_i(\lambda)$  is precalibrated and  $\mathbf{b}_j(\lambda)$  is trained from hyperspectral database.<sup>27</sup> So the hyperspectrum of the surface can be represented by  $J$  parameters  $\alpha_j$ .

The  $J$  sinusoidal patterns  $\{\mathbf{s}_i\}$  for Fourier domain multiplexing of  $J$  projected images  $\{\mathbf{x}_i\}$  are designed to have as minimal overlap in the Fourier domain as possible. Generally, the sinusoidal pattern can be written as

$$\mathbf{s}_i = 1 + \cos(\mathbf{p} \cdot \boldsymbol{\omega}_i), \quad (4)$$

where  $\mathbf{p}$  is the 2D spatial coordinate,  $\boldsymbol{\omega}_i$  ( $i = 1, 2, \dots, J$ ) represents the spatial frequency, and the Fourier transform of Eq. (4) includes three delta functions  $\delta(\boldsymbol{\omega} + \boldsymbol{\omega}_i)$ ,  $\delta(\boldsymbol{\omega})$ ,  $\delta(\boldsymbol{\omega} - \boldsymbol{\omega}_i)$  in the Fourier domain. After applying such sinusoidal modulation to the target scene, its spatial spectrum is duplicated into three replicas centered at  $\boldsymbol{\omega} = -\boldsymbol{\omega}_i$ ,  $\mathbf{0}$ ,  $\boldsymbol{\omega}_i$ , respectively. Research in the field of natural image statistics suggests that the Fourier domain of natural images is sparse<sup>30</sup> and enables efficient coding and sampling of natural images.<sup>25</sup> Taking advantage of this prior information, if the shifted distance  $\|\boldsymbol{\omega}_i\|$  is set properly, these three replicas can be separated to eliminate aliasing effectively. To set the sinusoidal patterns statistically, we first analyze the Fourier spectrum of natural scenes and then estimate the proper shift distance and the corresponding cropping size accordingly (details are discussed in Sec. 3).

The encoded image is recorded by the gray scale camera as

$$\mathbf{y} = \sum_{i=1}^J \mathbf{x}_i \odot \mathbf{s}_i. \quad (5)$$

In terms of reconstruction, we first transform the captured image  $\mathbf{y}$  to Fourier domain and demultiplexing each image by Fourier spectrum cropping and padding according to each sinusoidal pattern. After inverse Fourier transform to spatial domain, we obtain estimations of  $J$  spectral filtered images  $\{\hat{\mathbf{x}}_i\}$ . To further remove the aliasing, we use generalized alternating projection (GAP) to improve the reconstruction using these estimations as the initial value. GAP is basically an extended alternating projection algorithm which solves the compressive sensing problem in the transformed domain, i.e. discrete cosine transformation or wavelet domain.<sup>31,32</sup> The optimization problem is formulated as

$$\min_{\mathbf{W}} \|\mathbf{W}\|_{\ell_{2,1}^{\mathcal{G}, \beta}}, \quad \text{subject to } \mathbf{Y} = \mathbf{S}\mathbf{X} \quad \text{and} \quad \mathbf{X} = \mathbf{T}\mathbf{W}, \quad (6)$$

where the capital notation  $\mathbf{Y}$  and  $\mathbf{X}$  are vectorized forms of  $\mathbf{y}$  and  $\mathbf{x}$  [e.g.,  $\mathbf{Y} = \text{vec}(\mathbf{y})$ ,  $\mathbf{X} = \text{vec}(\mathbf{x})$ ], respectively.  $\mathbf{S} = [\mathbf{S}_1, \mathbf{S}_2, \dots, \mathbf{S}_J]$  with  $\mathbf{S}_i$  being diagonalization of vectorized form of  $\mathbf{s}_i$  [e.g.,  $\mathbf{S}_i = \text{diag}(\text{vec}(\mathbf{s}_i))$ ].  $\mathbf{T}$  is wavelet transformation matrix, and  $\mathbf{W}$  is corresponding coefficient in the transformed domain.

The  $\|\cdot\|_{\ell_{2,1}^{\mathcal{G}, \beta}}$  is weighted group- $\ell_{2,1}$  norm, calculated as

$$\|\mathbf{W}\|_{\ell_{2,1}^{\mathcal{G}, \beta}} = \sum_{k=1}^m \beta_k \|\mathbf{W}_{\mathcal{G}_k}\|_2, \quad (7)$$

where  $m$  is group number,  $\mathbf{W}_{\mathcal{G}_k}$  is a subvector of  $\mathbf{W}$  from  $k$ th group, with  $\mathcal{G}_k$  being components index and  $\beta_k$  being the group weight coefficient. The Eq. (6) would converge with desired accuracy after a number of iterations. After de-aliasing, we obtain estimations of six spectral-filtered images  $\{\hat{\mathbf{x}}_i\}$  with high quality.

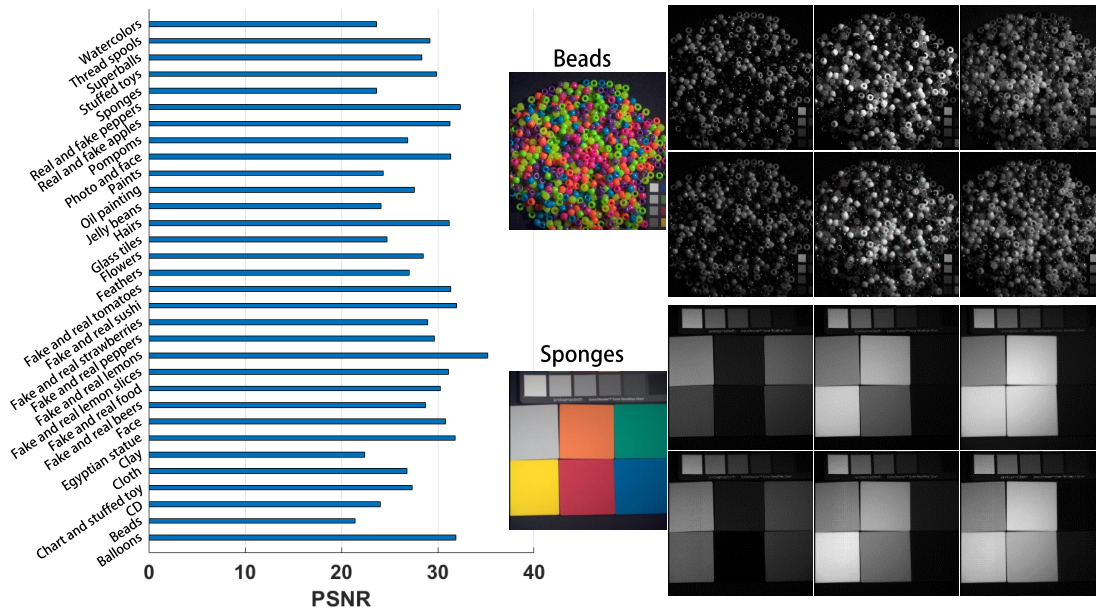


Figure 2. The PSNR of the reconstruction and two examples from the CAVE multi-spectral database. In each example, the upper row is the ground truth in 500 nm, 600 nm, and 700 nm, respectively and the lower row is the corresponding reconstruction.

To obtain the hyperspectral images, we inverse the linear system defined in Eq. (3) and get the following constrained optimization:

$$\arg \min_{\alpha} \|\hat{\mathbf{x}} - \mathbf{F}\alpha\|_2^2 + \eta \left\| \frac{\partial^2 \mathbf{r}(\lambda)}{\partial \lambda^2} \right\|_2^2 \quad \text{s.t.} \quad \mathbf{r}(\lambda) \geq 0. \quad (8)$$

Here  $\hat{\mathbf{x}} = [\hat{\mathbf{x}}_1, \hat{\mathbf{x}}_2, \dots, \hat{\mathbf{x}}_J]^T$ ,  $\alpha = [\alpha_1, \alpha_2, \dots, \alpha_J]^T$ , and  $\mathbf{F}_{ij} = \int_{\lambda} \mathbf{I}_i(\lambda) \mathbf{b}_j(\lambda) d\lambda$ . The parameter  $\eta$  weights the spectrum smoothness and we set  $\eta = 200$  in implementation empirically. This constrained optimization problem is solved with the quadratic programming solver in Matlab, which is based on the Lagrangian multiplier method.

### 3. SIMULATION AND EXPERIMENT

To evaluate the performance of our hyperspectral imaging system quantitatively, we test the imaging accuracy on the CAVE's multi-spectral image database. For each example, we simulate the encoded image based on the six sinusoidal patterns  $\{\mathbf{s}_i\}$  and CW's spectral responses  $\{\mathbf{I}_i\}$  demonstrated in Fig. 3(b). The reconstruction results are quite promising, with PSNR averagely over 28.4 dB, as shown in the left subfigure of Fig. 2. For a clearer demonstration, we also display two scenes with the lowest PSNR in the right part: Beads and Sponges, each with the ground truth (upper row) and corresponding reconstruction (lower row) displayed in comparison. We can see high fidelity reconstruction are achieved.

We build a prototype to verify our imaging scheme as shown in Fig. 3. The collimated broadband light is first modulated by a synchronized rotating color wheel (CW). The off-the-shelf six segment color wheel is driven by a high speed motor (a 60k rpm Walkera Super CP motor) and placed on the Fourier plane of the 4f system composed of L1 and L2 for spectral modulation. The spot on the color wheel is small enough so that the large temporary overlap between two segments can be neglected. Specifically, we use a DMD to modulate the binary approximation of gray scale sinusoidal patterns to achieve full modulation rate, and apply pinhole filtering on the Fourier plane to obtain ideal sinusoidal patterns. As for binarization, we choose dithering algorithm considering its low approximation error. In implementation, we use a single DMD to conduct binary patterning and Fourier-domain filtering simultaneously. The left part of the DMD modulates the incident light beam with a dithering sinusoidal pattern, and the right half of the DMD optically filters the spatial spectrum to remove the approximation error introduced by dithering algorithm [Fig. 3(c)]. The filter selects three dominant frequencies of an ideal sinusoidal pattern, i.e., -1, 0, and +1. Here the Fourier transform is taken by a concave mirror, which

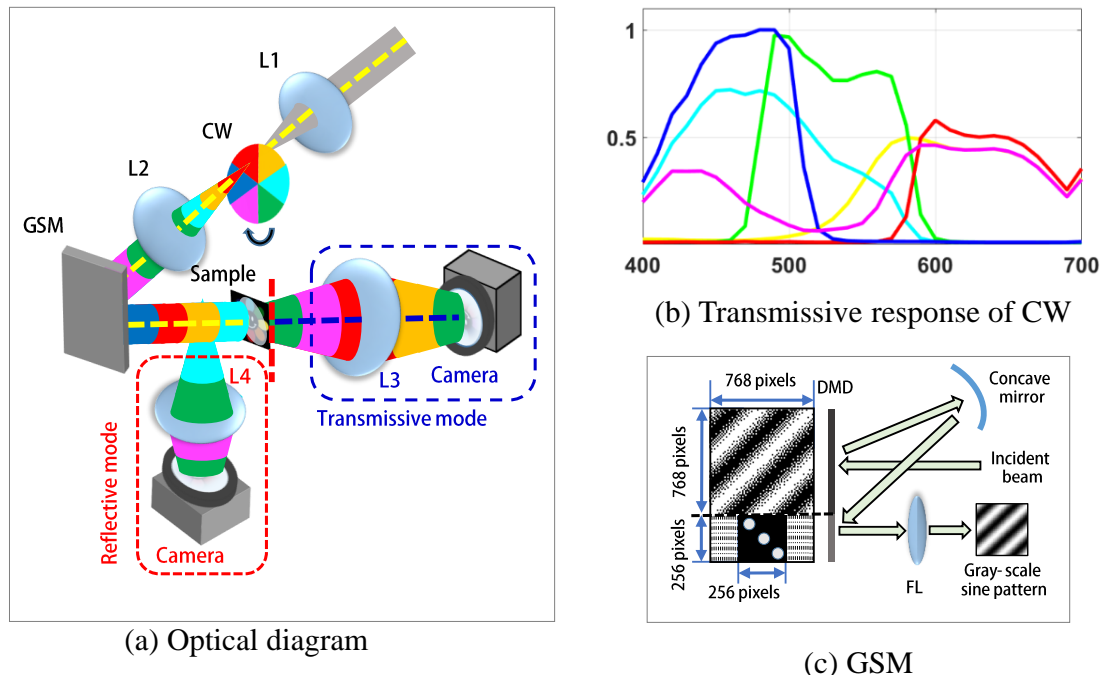


Figure 3. The imaging scheme of proposed method. (a) The optical diagram including transmissive and reflective mode (the beam splitter is omitted in reflective mode). L1 and L2: converging lens composing a 4f system. CW: color wheel. GSM: gray scale sinusoidal modulation. L3 and L4: Converging lens. (b) The transmissive response of CW. (c) The GSM module implementing fast gray scale sinusoidal modulation.

is well designed so that the right region of DMD is the Fourier plane of the left counterpart. This modulation can achieve 20 kHz gray scale sinusoidal patterning and is sufficient for our imaging scheme. As the refresh rate of gray scale DMD modulation is upper limited to 253 Hz (8 bit), we adopt the same method proposed in<sup>33</sup> to implement fast sinusoidal modulation for scalability, with the scheme illustrated in Fig. 3(c). After modulation, the light beam is focused by the converging lens onto the sample. Finally, the encoded sample information is collected by a gray scale camera (GO-5000C-USB, JAI) after converged by a lens.

To test the reconstruction accuracy of the hyperspectral images, we use a static color scene to evaluate our imaging system quantitatively. The test scene is strip-wisely uniform and we can calibrate the spectrum with a spectrometer. From the results in Fig. 4, we can see that the reconstructed spectrum of each patch after GAP optimization is of great consistency with the ground truth spectrum. We highlight the distinction after GAP optimization for clearer observation in the right part.

The second experiment is the diffusion process of two color pigments poured into a glass of water, captured in reflective the mode. We first pour the light blue pigment and then the orange one. The color of water gradually changes from light blue to orange, and eventually to the mixture of blue and orange. The spectrum distribution is changing over the diffusion process. We can also see the sinking and mixing process of these two color pigments in the water. We display three frames in Fig. 5 to show the dynamics. From the two reconstructions, we can clearly see that the proposed method can work well for hyperspectral imaging of dynamic scenes.

#### 4. SUMMARY AND DISCUSSIONS

In summary, we propose a snapshot hyperspectral imaging technique jointly utilizing the spectral and spatial redundancy of hyperspectral data cube. Specifically, we conduct spectral dimension reduction and spatial frequency multiplexing under the computational imaging scheme. For reconstruction, we can resolve spectral transmission/reflectance with low computational load in realtime. Benefiting from a recently proposed fast sinusoidal modulation<sup>34</sup> working at up to 20 kHz and a rotator working at 1 k revolution per second (rps), our imaging speed is mainly limited by the frame rate of the adopted camera and thus can work well for the common



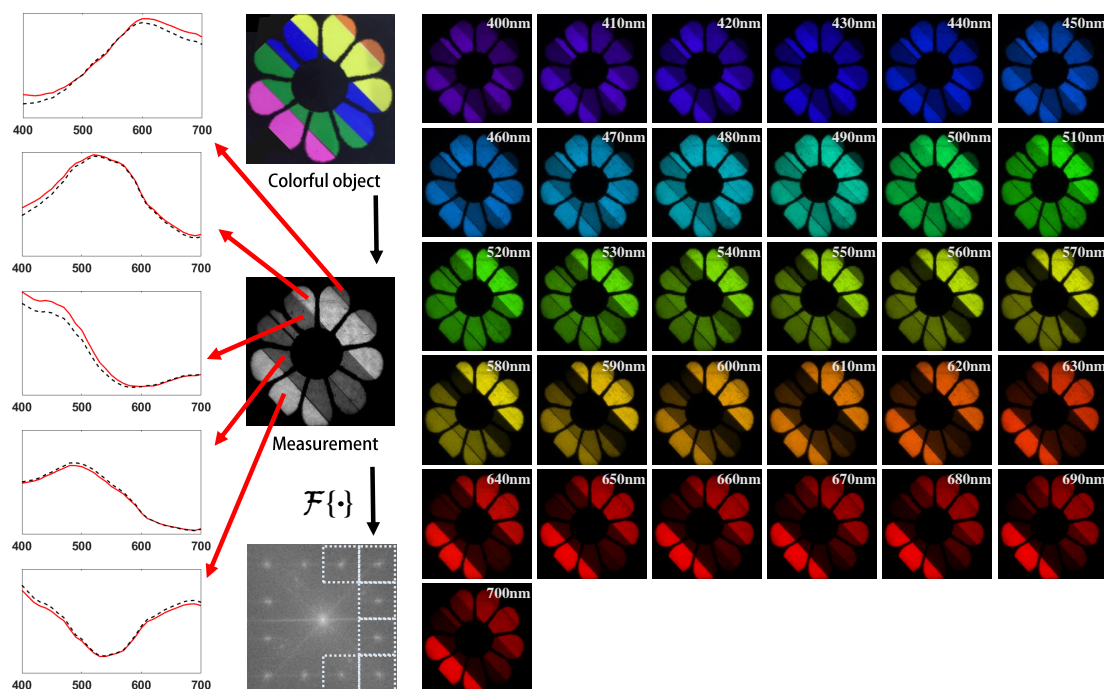


Figure 4. The experimental reconstruction of a flower film with five strips of different transparent color paper. The RGB image of the object, the measurement together with its Fourier space and the reconstructed five spectrum of transparent color paper are displayed in the left part. The solid red and dashed black curves are the true spectrum and reconstruction, respectively. The reconstructed hyperspectral images are displayed in the right. The spectral range is 400 nm ~ 700 nm.

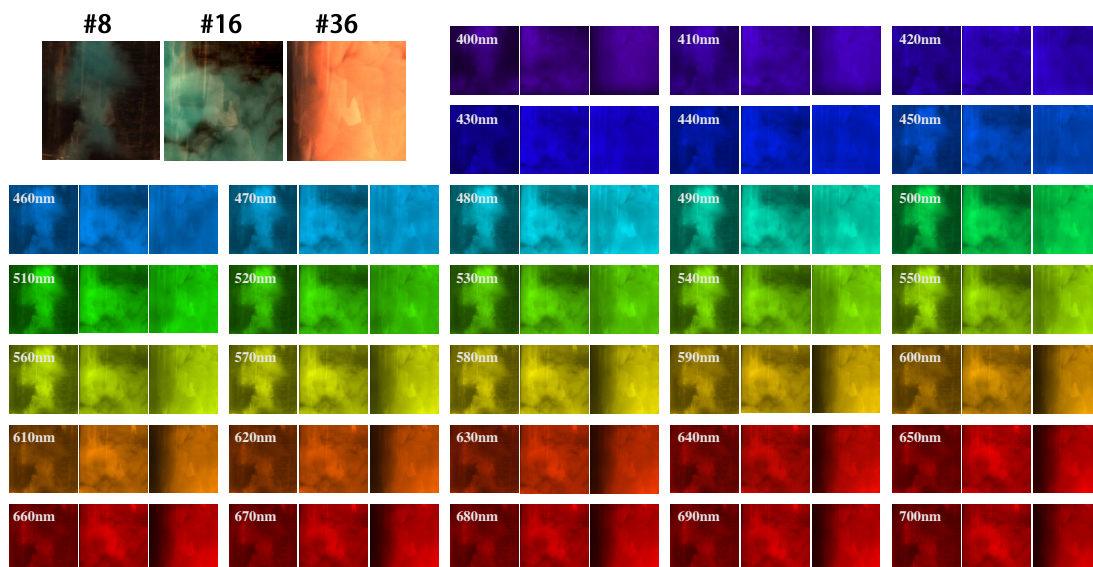


Figure 5. Hyperspectral reconstruction of the diffusion process of color pigments poured into clean water. Three out of 77 frames are displayed.

dynamic scenes. Moreover, utilizing the temporal redundancy of natural scenes, imaging speed can be further improved by introducing random modulation based on compressive sensing.<sup>35–39</sup> In short, our technique is quite promising to be extended to a high performance hyperspectral imaging system.

## Funding

The National key foundation for exploring scientific instrument of China No.2013YQ140517; The National Science Foundation of China under Grant 61327902 and Grant 61631009.

## REFERENCES

- [1] M. T. Eismann, C. R. Schwartz, J. N. Cederquist, J. A. Hackwell, and R. J. Huppi, "Comparison of infrared imaging hyperspectral sensors for military target detection applications," *Proc. SPIE* **2819**, 91–102(1996).
- [2] J. P. Ardouin, J. Lévesque, and T. A. Rea, "A demonstration of hyperspectral image exploitation for military applications," in *Proceedings of IEEE Conference on Information Fusion (IEEE, 2007)*, pp. 1–8.
- [3] S. Delalieux, A. Auwerkerken, W. W. Verstraeten, B. Somers, R. Valcke, S. Lhermitte, J. Keulemans, and P. Coppin, "Hyperspectral reflectance and fluorescence imaging to detect scab induced stress in apple leaves," *Remote Sens.* **1**, 858–874 (2009).
- [4] V. Backman, M. B. Wallace, L. Perelman, J. Arendt, R. Gurjar, M. Müller, Q. Zhang, G. Zonios, E. Kline, T. McGillican, S. Shapshay, T. Valdez, K. Badizadegan, J. M. Crawford, M. Fitzmaurice, S. Kabani, H. S. Levin, M. Seiler, R. R. Dasari, I. Itzkan, J. Van Dam and M. S. Feld "Detection of preinvasive cancer cells," *Nature* **406**, 35–36 (2000).
- [5] G. Zavattini, S. Vecchi, G. Mitchell, U. Weisser, R. M. Leahy, B. J. Pichler, D. J. Smith, and S. R. Cherry, "A hyperspectral fluorescence system for 3D in vivo optical imaging," *Phys. Med. & Biol.* **51**, 2029 (2006).
- [6] R. T. Kester, N. Bedard, L. Gao, and T. S. Tkaczyk, "Real-time snapshot hyperspectral imaging endoscope," *J. Biomed. Opt.* **16**, 056005–056005 (2011).
- [7] T. Vo-Dinh, "A hyperspectral imaging system for in vivo optical diagnostics," *IEEE Eng. Med. Biol. Mag.* **23**, 40–49 (2004).
- [8] M. J. Barnsley, J. J. Settle, M. A. Cutter, D. R. Lobb, and F. Teston, "The proba/chris mission: A low-cost smallsat for hyperspectral multiangle observations of the earth surface and atmosphere," *IEEE Tran.on Geosci. Remote Sens.* **42**, 1512–1520 (2004).
- [9] J. P. Bibring, Y. Langevin, A. Gendrin, B. Gondet, F. Poulet, M. Berthé, A. Soufflot, R. Arvidson, N. Mangold, J. Mustard, P. Drossart, and the OMEGA team, "Mars surface diversity as revealed by the omega/mars express observations," *Science* **307**, 1576–1581 (2005).
- [10] Z. Pan, G. Healey, M. Prasad, and B. Tromberg, "Face recognition in hyperspectral images," *IEEE Trans. on Pattern Anal. and Machine Intelligence* **25**, 1552–1560 (2003).
- [11] D. J. Brady, *Optical imaging and spectroscopy* (John Wiley & Sons, 2009).
- [12] G. R. Arce, D. J. Brady, L. Carin, H. Arguello, and D. S. Kittle, "Compressive coded aperture spectral imaging: An introduction," *IEEE Signal Processing Magazine* **31**, 105–115 (2014).
- [13] L. Weitzel, A. Krabbe, H. Kroker, N. Thatte, L. Tacconi-Garman, M. Cameron, and R. Genzel, "3d: The next generation near-infrared imaging spectrometer," *Astronomy and Astrophysics Supplement Series* **119**, 531–546 (1996).
- [14] N. Hagen and M. W. Kudenov, "Review of snapshot spectral imaging technologies," *Optical Engineering* **52**, 090901–090901 (2013).
- [15] J. D. Matchett, R. I. Billmers, E. J. Billmers, and M. E. Ludwig, "Volume holographic beam splitter for hyperspectral imaging applications," *Proc. SPIE* **6668**, 66680K (2007).
- [16] A. Gorman, D. W. Fletcher-Holmes, and A. R. Harvey, "Generalization of the lyot filter and its application to snapshot spectral imaging," *Optics Express* **18**, 5602–5608 (2010).
- [17] A. R. Harvey and D. W. Fletcher-Holmes, "High-throughput snapshot spectral imaging in two dimensions," *Proc. SPIE* **4959**, 4959136 (2003).
- [18] M. W. Kudenov, M. E. Jungwirth, E. L. Dereniak, and G. R. Gerhart, "White-light sagnac interferometer for snapshot multispectral imaging," *Applied Opt.* **49**, 4067–4076 (2010).
- [19] T. Okamoto and I. Yamaguchi, "Simultaneous acquisition of spectral image information," *Optics Letters* **16**, 1277–1279 (1991).
- [20] A. Hirai, T. Inoue, K. Itoh, and Y. Ichioka, " Application of multiple-image fourier transform spectral imaging to measurement of fast phenomena," *Optical Review* **1**, 205–207 (1994).



- [21] L. Gao, R. T. Kester, and T. S. Tkaczyk, "Compact image slicing spectrometer (iss) for hyperspectral fluorescence microscopy," *Optics Express* **17**, 12293–12308 (2009).
- [22] M. W. Kudenov and E. L. Dereniak, "Compact snapshot birefringent imaging fourier transform spectrometer," *Proc. SPIE* **7812**, 06–12 (2010).
- [23] M. Gehm, R. John, D. Brady, R. Willett, and T. Schulz, "Single-shot compressive spectral imaging with a dual-disperser architecture," *Optics Express* **15**, 14013–14027 (2007).
- [24] A. Chakrabarti and T. Zickler, "Statistics of real-world hyperspectral images," in *Proceedings of IEEE Conference on Computer Vision and Pattern Recognition (IEEE, 2011)*, pp. 193–200.
- [25] L. Bian, J. Suo, X. Hu, F. Chen, and Q. Dai, "Efficient single pixel imaging in fourier space," *Journal of Optics* **18**, 085704 (2016).
- [26] F. Yasuma, T. Mitsunaga, D. Iso, and S. K. Nayar, "Generalized assorted pixel camera: postcapture control of resolution, dynamic range, and spectrum," *IEEE Trans. Image Process.* **19**, 2241–2253 (2008).
- [27] J. P. Parkkinen, J. Hallikainen, and T. Jaaskelainen, "Characteristic spectra of munsell colors," *J. Opt. Soc. Am. A* **6**, 318–322 (1989).
- [28] J. I. Park, M. H. Lee, M. D. Grossberg, and S. K. Nayar, "Multispectral imaging using multiplexed illumination," in *Proceedings of IEEE Conference on Computer Vision (IEEE, 2007)*, pp. 1–8.
- [29] S. Han, I. Sato, T. Okabe, and Y. Sato, "Fast spectral reflectance recovery using dlp projector," in *Proceedings of Asian Conference on Computer Vision*, (Springer, 2010), pp. 323–335.
- [30] M. Rabbani, "JPEG2000: Image compression fundamentals, standards and practice," *Journal of Electronic Imaging* **11**, 286 (2002).
- [31] X. Liao, H. Li, and L. Carin, "Generalized alternating projection for weighted-2,1 minimization with applications to model-based compressive sensing," *SIAM Journal on Imaging Sciences* **7**, 797–823 (2014).
- [32] X. Yuan, "Generalized alternating projection based total variation minimization for compressive sensing," in *Proceedings of IEEE International Conference on Image Processing (IEEE, 2016)*, pp. 2539–2543.
- [33] Y. Zhang, J. Suo, Y. Wang, and Q. Dai, "Doubling the pixel count limitation of single-pixel imaging via sinusoidal amplitude modulation," *Optics Express* **26**, 6929–6942 (2018).
- [34] Z. Zhang, S. Liu, J. Peng, M. Yao, G. Zheng, and J. Zhong, "Simultaneous spatial, spectral, and 3d compressive imaging via efficient fourier single-pixel measurements," *Optica* **5**, 315–319 (2018).
- [35] Y. Hitomi, J. Gu, M. Gupta, T. Mitsunaga, and S. K. Nayar, "Video from a single coded exposure photograph using a learned over-complete dictionary," in *Proceedings of IEEE International Conference on Computer Vision (IEEE, 2011)*, pp. 287–294.
- [36] J. Holloway, A. C. Sankaranarayanan, A. Veeraraghavan, and S. Tambe, "Flutter shutter video camera for compressive sensing of videos," in *Proceedings of IEEE International Conference on Computational Photography*, (IEEE, 2012), pp. 1–9.
- [37] P. Llull, X. Liao, X. Yuan, J. Yang, D. Kittle, L. Carin, G. Sapiro, and D. J. Brady, "Coded aperture compressive temporal imaging," *Optics Express* **21**, 10526–10545 (2013).
- [38] D. Reddy, A. Veeraraghavan, and R. Chellappa, "P2c2: Programmable pixel compressive camera for high speed imaging," in *Proceedings of IEEE Conference on Computer Vision and Pattern Recognition (IEEE, 2011)*, pp. 329–336.
- [39] X. Yuan, P. Llull, X. Liao, J. Yang, D. J. Brady, G. Sapiro, and L. Carin, "Low-cost compressive sensing for color video and depth," in *Proceedings of the IEEE Conference on Computer Vision and Pattern Recognition (IEEE, 2014)*, pp. 3318–3325.